Regulatory architecture and standing variation drive parallelism in floral evolution

Kevin Sartori[1,†], Natalia Wozniak[2,†], Anahid Powell[2,†], Ushio Fujikura[2], Christian Kappel[2], Tian-Feng Lü[3,4], Yang Dong[3,4], Stefanie Rosa[1], Michael Lenhard[2] and Adrien Sicard[1*]

[1] Uppsala Biocenter, Department of Plant Biology, Swedish University of Agricultural Sciences, BOX 7080, 750 07, Uppsala, Sweden
[2] Institut für Biochemie und Biologie, Universität Potsdam, Karl-Liebknecht-Str. 24-25, 14476 Potsdam-Golm, Germany
[3] State Key Laboratory of Plant Diversity and Specialty Crops, Institute of Botany, Chinese Academy of Sciences, 20 Nanxincun, Xiangshan, Beijing 100093, China
[4] China National Botanical Garden, Beijing 100093, China

*Corresponding author: Adrien Sicard (adrien.sicard@slu.se)

†These authors contributed equally

Abstract

Evolution repeatedly gives rise to similar phenotypes, suggesting that constraints and biases make some evolutionary trajectories more likely than others, yet the mechanisms underlying this predictability remain poorly understood. Using repeated transitions to self-fertilization in a model Brassicaceae genus, we show that independent reductions in petal size arise from dosage changes at the same pleiotropic growth regulator, *JAGGED* (*JAG*). Petal development exhibits particularly high sensitivity to *JAG* dosage, resulting in organ-specific morphological shifts with minimal effects on other organs and limited pleiotropy. In both selfing species, these changes were drawn from functionally divergent variants whose polymorphism patterns are consistent with long-term maintenance under weak selection. Our results demonstrate how developmental network architecture and the maintenance of functional variation at pleiotropic loci combine to channel evolution toward predictable outcomes.

Main

Evolution often produces similar traits across unrelated lineages, suggesting that outcomes are shaped by predictable constraints rather than chance. Such convergent phenotypes often arise in species exposed to similar ecological pressures, implying that adaptive solutions are limited [1]. Beyond ecology, developmental constraints within Gene Regulatory Networks (GRNs) also restrict the range of viable phenotypes [2,3]. Because GRNs carry historical legacies, closely related species often share the same constraints and thus respond similarly to shifts in selection pressures [4]. Although specific cases of genetic convergence have been identified, the general mechanisms that drive repeated phenotypic evolution remain poorly understood [5].

Cross-pollination is common in plants and often enforced by self-incompatibility systems, which make reproduction dependent on animal pollinators [6–10]. To attract pollinators, plants invest in large floral displays [11–13]. Yet self-incompatibility has repeatedly broken down throughout evolution, producing self-fertilizing (selfing) lineages, likely as reproductive assurance when mates are scarce [14]. Remarkably, independent transitions to selfing often converge on similar floral changes, collectively termed the selfing syndrome, with a hallmark being a pronounced reduction in flower and petal size [6,14]. Genetic studies indicate that floral traits often evolve independently from one another or from vegetative traits, suggesting adaptive changes targeting specific organ dimensions [15–23]. Yet because most growth regulators in plants are pleiotropic, influencing multiple organs [24], such specific changes likely depend on rare organ-specific regulators or on regulatory elements within pleiotropic genes. It remains, nevertheless, unclear which general growth regulators can be modulated at an organ-specific level and how such targeted changes in organ size occur. If such a regulation is limited, it could help explain phenotypic convergence following transitions to selfing. Beyond pleiotropy, the effect size and availability of adaptive variation in ancestral populations may further constrain evolution [25].

In this study, we exploit the *Capsella* genus as a model to study the convergent evolution of flowers after independent transitions to selfing [26–33]. In this genus, the selfing species *C. rubella* (*Cr*) and *C. orientalis* (*Co*) evolved independently from an outcrossing *C. grandiflora* (*Cg*)-like ancestor following the breakdown of self-incompatibility, diverging ~100 kya and within the last 2 million years, respectively (**Fig. 1a**) [28,34–36]. Both exhibit a fully established selfing syndrome, including a pronounced reduction in petal size (**Fig. 1)** [37].

Convergent petal size reduction via similar reduction of distal cell proliferation

A major phenotypic change in *Cr* and *Co* is a pronounced reduction in petal size, accompanied by fewer cells, implicating altered cell proliferation as a central mechanism [38]. To examine the developmental basis of these changes, we analyzed cellular patterns along the proximal-distal axis of petals, incorporating various descriptors of cell shape and directional growth (**Extended Data Table 1**). Petals exhibit two distinct cell clusters. A proximal cluster of large, elongated cells and a distal cluster of small, rounded cells, separated by a transition zone where cell size and anisotropy gradually decrease (**Fig. 1B and Extended Data Fig. 1**). While this pattern is largely conserved across species, cellular features along this axis can distinguish the petals of selfers from those of the outcrosser (one-way ANOVA: $F(1,13) = 28.54$, $p = 0.00013$, $\eta^2 = 0.687$) (**Fig. 1b, 1d, and Extended Data Fig. 1, and 2**). Selfers differ primarily in the distal region, where cell number is reduced roughly five-fold compared to the outcrosser, resulting in a two-fold reduction in length and a three-fold decrease in width (**Fig. 1e and Extended Data Fig. 1c; Extended Data Table 2**). Early petal growth occurs via cell proliferation, which initially takes place throughout the primordia. Once the petal primordia reach approximately 90 µm in length, proliferation rapidly becomes restricted to the distal region, thereby determining the size of the distal section, while cell elongation is largely confined to the proximal domain (**Fig. 1 and Extended Data Fig.3**). In selfers, cell proliferation in the distal margin, as judged from the number of S-phase cells, is reduced three- to four-fold relative to the outcrosser, consistently across both lineages (**Fig. 1f and 1g**). Thus, despite independent origins, petal size reduction in these selfing species arises through the same developmental mechanism: restricted growth at the distal margin due to decreased cell division.

Independent selfing lineages co-opted *JAG* to reduce petal size

The convergence in petal development suggests that similar genetic mechanisms underlie size reduction in the two selfing species. Previous studies indicated that half of the loci associated with petal size are shared between *Cr* and *Co*, with PAQTL2 on chromosome 2 contributing most to phenotypic evolution (**Extended Data Fig. 4a**) [38,39]. To refine the location of PAQTL2 in each selfing species, we introgressed the outcrossing *Cg* alleles into each selfer, creating near-isogenic lines (*NILrg1* and *NILog2*) and screened for recombinants within this region (**Fig. 2**). By analyzing petal size segregation in the progeny, we narrowed down the causal mutation (s) to 14.6 kb in *Cr* and 130 kb in *Co*. The most informative recombinants from *NILrg1* indicated that the causal

97 mutation(s) are situated between 9,061,779 and 9,076,392 bp on chromosome 2. We confirmed
98 this region by generating a quasi-isogenic line (*qILrg*) for the 14.6-kb interval, where *Cr*
99 homozygotes exhibited ~20% smaller petals than *Cg* homozygotes, recapitulating the PAQTL2
100 effect (**Extended Data Fig. 4c and 7a**). In *NILog2*, the most informative recombinant localized
101 the causal mutation to 9,019,066–9,149,619 bp on chromosome 2, accounting for a 25% petal
102 reduction in *Co* (**Fig. 2b and Extended Data Fig. 7a**). This region overlaps with the locus
103 identified in *Cr*, confirming that the same genomic locus underpins PAQTL2 in both selfing
104 species.
105 The 14.6-kb interval contained only two genes, including the *Arabidopsis thaliana JAGGED*
106 (*JAG*) ortholog, a zinc-finger transcription factor, known to control lateral organ growth and distal
107 cell proliferation (**Fig. 2a**) [40]. In an EMS-mutagenized *C. rubella* screen, we identified a mutant
108 phenocopying the *A. thaliana jag* mutation (**Extended Data Fig. 6a**)[40]. Bulked-segregant analysis
109 revealed a splice-site mutation in the third exon of *JAG*, preventing proper splicing and introducing
110 a premature stop codon (**Extended Data Fig. 5**). The defect was rescued by reintroducing a wild-
111 type *Cr* allele, confirming *JAG* inactivation as causal (**Extended Data Fig. 6b**). We thus used this
112 mutant in a quantitative complementation test [41] to test whether *JAG* underlies PAQTL2 in both
113 selfers. In this assay, natural alleles were crossed to a jag+/– background, where functional
114 differences between the natural alleles are expected to be amplified only when the loss-of-function
115 mutation affects the same gene. Consistently, in both cases, the differences between the selfer and
116 outcrosser alleles were stronger when combined with the mutant alleles (**Fig. 2c and d**). Linear
117 model analysis revealed a significant interaction between the tested (*Cg1* and *Cr* or *Cg2* and *Co*)
118 and control allele (WT and *crjag*) (β = -0.38976 ± 0.08710, t = -4.475, $p = 8.56 \times 10^{-6}$ for *NILog*;
119 and β = 0.311 ± 0.043, t = 7.245, $p = 2.27 \times 10^{-12}$ for *qILrg*), indicating that polymorphism within
120 *JAG* contributed to a reduction in petal size in both cases. To further confirm *JAG's* role, we
121 transformed genomic constructs corresponding to the *Cg* (*JAGg1*) and *Cr* (*JAGr*) alleles
122 segregating in *NILrg*, as well as the *Cg* (*JAGg2*) and *Co* (*JAGo*) alleles from *NILog*, into the *A.*
123 *thaliana jag-2* mutant (**Extended Data Fig. 4d and e**). All alleles rescued the mutant phenotype,
124 but *Cg1* and *Cg2* alleles produced larger petals than *Cr* and *Co* alleles, respectively. These results
125 further support that allelic variation in *JAG* underlies convergent petal size reduction in both
126 selfing species.

127 ***JAG* is essential to promote distal petal cell proliferation**

128 Inactivation of *JAG* in *Cr* causes pleiotropic effects, leading to a ≥10% reduction in the size of
129 most organs, with particularly strong effects on leaves (30%), petals (60%) (**Extended Data Fig.**
130 **6**), and fruit [42]. To uncover the developmental basis, we compared wild-type and *crjag* petals.
131 Silhouette overlays showed that the proximal petal region was largely unaffected, whereas the
132 distal region was almost entirely missing (**Fig. 3a and 3b**). Cellular analysis revealed a ~5-fold
133 reduction in total cell number (**Fig. 3c and 3d**). This reduction in cell number was particularly
134 pronounced in the transition and distal zones (**Fig. 3d**). Cell elongation in the proximal region and
135 the position of the transition zone were largely unaffected, indicating that overall petal growth
136 patterning is not altered by *JAG* (**Fig. 3b**). However, growth in the marginal part of the petal was
137 almost completely abolished, with only a few small rounded cells formed within the distal area.
138 This was associated with more than a twofold reduction in the number of cell proliferation events
139 at the onset of cell proliferation within the distal part of the petal primordia (**Fig. 3e and f**).
140 Together, these results indicate that *JAG* is essential for promoting and maintaining a high rate of
141 cell proliferation at the petal margin. Lack of function almost completely abolishes growth in the
142 distal region. These observations suggest that *JAG* does not affect the overall growth pattern of the
143 petal but instead promotes cell proliferation within the distal margin, providing strong support for
144 its proposed function as a distal growth promoter during petal development [43] and explaining the
145 cellular basis of convergent petal size reductions in *Capsella* (**Fig. 1**).

146 **Cis-regulatory changes in *JAG* drive petal size reduction in selfing *Capsella* species**

147 To assess the impact of allelic variation at *JAG*, we compared petal morphology in the *NILog* and
148 *qILrg* lines (**Fig. 4 a-d**). Consistent with the loss of *JAG* function, both showed a selective
149 reduction in distal petal growth, with total petal area decreased by 22% and 15%, respectively
150 (**Extended Data Fig. 7**). This reduction reflected a lower total cell number, most pronounced at
151 the distal tip. Strikingly, the effect was specific to petals; other floral organs and leaves were
152 unaffected, in contrast to the broad reductions seen in *crjag*. These results suggest that *JAG* activity
153 has been selectively modified during petal development.
154 Among the polymorphisms distinguishing the tested *JAG* alleles, four resulted in amino acid
155 substitutions, but none affected conserved regions or the C2H2 zinc-finger domain. Furthermore,
156 promoter-swap experiments revealed a cis-regulatory basis. *A. thaliana jag-2* mutants transformed
157 with the *Cr* coding sequence under the *Cg1* promoter (*pJAGg1::JAGr*) developed significantly

158 larger petals than those carrying the reciprocal construct (*pJAGr::JAGg1*) (Fig. S4 D). Moreover,
159 *jag-2*; *pJAGr::JAGg1* petals were similar in size to *jag-2*; *JAGr* petals and significantly smaller
160 than *jag-2*; *JAGg1* petals (**Extended Data Fig. 4**). Thus, in *Cr*, differences in *JAG* activity are
161 explained by cis-regulatory rather than protein-coding changes. Because both selfers share the
162 same non-synonymous substitutions, these are unlikely to contribute in Co, also suggesting cis-
163 regulatory evolution in this species.

164 **Subtle changes in *JAG* dosage drive petal size evolution with minimal pleiotropy**

165 Single-cell analysis revealed reduced *JAG* expression in both developing leaves and petals of the
166 selfers compared to the outcrosser (**Extended Data Fig. 8**). Because *JAG* promotes cell division
167 [44], its reduced activity likely explains the lower proliferation observed at the petal margin. Yet,
168 only petals showed strong size reduction, suggesting heightened sensitivity to *JAG* dosage. This is
169 consistent with the severe petal defects of *jag* mutants and the established role of *JAG* in driving
170 distal petal growth.
171 To test whether *JAG* dosage could explain petal size differences, we used an existing petal growth
172 model based on the Growing Polarized Tissue (GPT) framework [45] (**Extended Data Fig. 9**). In
173 this model, tissue polarity is generated by diffusion of a polariser (POL) produced by the basal
174 organiser (PROXORG), which drives growth along the proximal-distal axis (Kpar). The distal
175 factors (DGRAD, DISTORG) promote lateral (Kper) and divergent growth from the petal midline,
176 respectively. The model reproduces *A. thaliana* petals and is consistent with *JAG* functioning as
177 DGRAD, with the phytohormone auxin signalling contributing to the polarity field establishment
178 [45]. However, it failed to capture *Capsella* petal shapes (**Extended Data Fig. 9**). Adjusting the
179 model by broadening DGRAD and DISTORG domains and allowing DGRAD to also influence
180 Kpar yielded realistic *Cg* petals (**Fig. 4, Extended Data Fig. 9 and Methods**). With this new
181 model, the complete loss of DGRAD, combined with fragmented auxin distribution (as in [45]),
182 produced short and narrow 'jagged' petals phenocopying the *crjag* mutants. Quantitative tuning
183 showed that even modest reductions in *JAG* activity had strong effects on petal size. A 10%
184 decrease in its effects on Kper and Kpar led to a 23% reduction in petal size, while a 25% reduction
185 in *JAG* resulted in more than a twofold decrease in petal size (**Fig. 4e)**.
186 To test whether organ-specific sensitivity could explain the minimal pleiotropy of change in *JAG*
187 expression, we next used an existing leaf growth model [46] (**Extended Data Fig. 10**). In this
188 framework, a PGRAD gradient along the proximal-distal axis regulates growth parallel to the axis

(Kpar), while the broadly expressed factor LAM promotes perpendicular growth (Kper), which is further inhibited by MID along the central axis. At later stages, LATE reduces Kpar and enhances Kper activation by LAM. Because *crjag* leaves show a 14% reduction in length and 18% in width, we hypothesised that *JAG* contributes to both PGRAD and LAM activity, consistent with its expression at proximal side of leaf and sepal margins [40,47,48]. Calibrating the model to match the *crjag* phenotype and running both the petal and leaf models for a similar number of iterations under different *JAG* dosage revealed that petals were far more sensitive to *JAG* reduction. At 75% activity, petal area had already decreased by ~30%, whereas leaf area was reduced by less than 15%, and this contrast becomes even stronger at lower dosage levels (**Extended Data Fig. 10**). This analysis shows that modest decreases in *JAG* activity strongly affect petal growth but have only minor effects on other organs. Such heightened sensitivity may represent a developmental constraint and help explain why *JAG* has been repeatedly co-opted to reduce petal size in different lineages. Because *JAG* plays a central role in promoting petal growth while contributing less to other organs, even subtle changes in its activity can drive major evolutionary shifts in petal morphology with minimal pleiotropic consequences.

Standing variation facilitates parallel petal size evolution

A notable observation was that polymorphisms affecting *JAG* function in both selfing lineages showed similar overdominant effects (**Fig. 5**). In both *NILog* and *qILrg* heterozygotes had significantly larger petals than homozygotes (effect sizes of 0.342 and 0.186 mm^2; SE = 0.132 and 0.0871; df = 19 and 20; t = 2.582 and 2.136; Bonferroni-adjusted p = 0.0183 and 0.0452, respectively). Similarly, in complementation crosses, *Cg/crjag* heterozygotes produced larger petals than *Cg/Cr* heterozygotes (**Fig. 2**). *JAG*, therefore, appears to be prone to overdominant mutations, likely due to dosage-sensitive responses in petal development.

Such overdominance, if maintained by selection, could promote allele reuse by keeping functionally divergent variants in the outcrosser population. To test this, we examined allele frequencies across natural populations at polymorphic sites segregating between the haplotypes used in transgenic assays (*Cg1- Cr* and *Cg2 - Co*). Of 642 polymorphic sites, 84 converged between selfers. Yet, none of these sites were fixed, as selfer alleles still occurred at ≥4% in *Cg*. This lack of strong differentiation excludes a scenario of parallel evolution via identical independent changes at the same locus post-divergence. Both selfers also carried species-specific alleles (16 in *Cr*, 26 in *Co*), indicating that independent de novo changes may also have contributed

(**Extended Data Fig. 11**). Because the high number of convergent polymorphisms suggested evolution via standing genetic variation, we tested whether selfer/outcrosser polymorphisms segregating in *Cg* were associated with petal size (**Fig. 5 and Extended Data Fig. 12**). Among 233 polymorphisms with sufficient genotype counts, 15 were significantly correlated with petal length (FDR-adjusted $P < 0.05$). Of these, nine showed overdominance, with heterozygotes having larger petals. Six of these nine were fixed in both selfers, and five were associated with smaller petals (**Extended Data Fig. 12**). This suggests that collateral evolution through the fixation of multiple small-effect variants could also contributed to petal size reduction.

Because *Cg/Cr* and *Co* lineages diverged approximately 1 Mya, this scenario implies that these polymorphisms have persisted for thousands of generations (**Fig. 1**, [49,50]). Such persistence could plausibly be explained by heterozygote advantage, given the importance of petal size for pollinator attraction. However, none of the convergent overdominant polymorphisms showed significant deviations from Hardy-Weinberg equilibrium (HWE) or evidence of heterozygote excess in *Cg* (**Extended Data Fig. 13**). Nonetheless, in a population with a large effective population size, such as *Cg* [51], weak overdominant selection could maintain allele frequencies near a stable equilibrium without causing apparent departure from HWE [52]. To test this hypothesis, we estimated selection coefficients acting on petal morphology by correlating petal size with reproductive efficiency in a hybrid outcrossing population (**Extended Data Fig. 13b**). Using these estimates, together with the observed heterozygote effects, we modelled allele trajectories for each convergent overdominant polymorphism (**Extended Data Fig. 13c**). Despite low selection coefficients (average s against homozygotes ≈ 0.0056), overdominant selection was sufficient to maintain these polymorphisms over millions of generations (probability of heterozygote maintenance: 1 with selection and drift vs. 0.18 under drift alone) (**Extended Data Fig. 13c**). Consistent with our above analysis, only rare simulations (<0.05%) led to HWE departures. Together, these results indicate that weak overdominant selection can maintain functionally divergent alleles at polymorphic frequencies in large outcrossing populations, thereby enabling repeated recruitment of standing variation and facilitating phenotypic convergence through collateral evolution.

Implications for convergent evolution of selfing lineages

Petal reduction in both *Capsella* selfers arose through the identical developmental mechanism and the co-option of the same genetic solution (**Extended Data Fig. 14**). In both lineages, cis-regulatory changes reduce the activity of *JAG*, a general growth promoter, leading to decreased

251 cell proliferation in the distal petal margin. Although reduced *JAG* expression is detectable in
252 several organs, only petals are strongly affected, likely because petal growth is more sensitive to
253 *JAG* dosage. This heightened sensitivity appears to impose a developmental constraint on
254 evolution by enabling large morphological changes in petals while limiting pleiotropic effects,
255 explaining at least in part gene reuse and the convergent evolution observed between independent
256 transitions to self-fertilisation. In addition, the reuse of standing variation also appears to have
257 facilitated phenotypic parallelism. Variants segregating at intermediate frequency in *Cg*, where
258 they influence petal size, have been similarly fixed in both selfing lineages. Weak overdominant
259 selection associated with improved pollinator attraction explains the long-term persistence of these
260 variants in *Cg,* and thus their repeated use. Together, our findings illustrate how the interplay
261 between standing genetic variation and developmental constraints interact to bias evolutionary
262 trajectory toward repeatable outcomes.

263 # Methods

264 ## Plant material

265 This study used *Capsella rubella*, *C. orientalis*, and *C. grandiflora* accessions previously described
266 by [37]. Near-isogenic lines (NILs) segregating for PAQTL_2 were generated by introgressing the
267 *Cg926* allele into *Cr1504* (*NILrg*) and *Co1983* (*NILgo*) through five and three rounds of
268 backcrossing, respectively, followed by two additional generations of selfing while maintaining
269 heterozygosity at the PAQTL_2 locus. Progeny from these two NILs were used for fine mapping.
270 The crossing scheme used to generate the quasi-isogenic line (qILrg) is shown in **Extended Data**
271 **Fig. 4c**.
272 The *jag-2* EMS mutant in *Landsberg-erecta* (L-*er*) background showing recessive floral phenotype
273 was previously identified to have a single nucleotide change (C/T) in the second exon resulting in
274 a premature stop codon [40]. Here, we have identified the *Crjag* mutant in *C. rubella Cr22.5*
275 background by screening a *C. rubella* (*Cr22.5*) ethyl-methanesulfonate (EMS) mutagenized
276 population for plants with reduced petal size [53]. The genetic basis and phenotypic characterization
277 of this mutant are presented in this manuscript.

278 **Growth conditions**

279 Seeds were surface-sterilized, plated on half-strength Murashige-Skoog medium supplemented
280 with gibberellic acid (Duchefa Biochemie; 3.3 mg/L GA), and vernalized for two days at 4°C.
281 Germination occurred at 22°C for ten days. To initiate the transition to flowering, seedlings were
282 placed at 4°C for ten days. Subsequently, plants were grown in a growth chamber under long-day
283 conditions (16 hours light/8 hours dark) with a temperature cycle of 22°C during the day and 16°C
284 at night, 70% humidity, and a light intensity of 150 µmol $m^{-2}s^{-1}$.

285 **Morphological measurements**

286 To characterize the effect of PAQTL_2, diverse genetic constructs, and *jag* mutations, sizes of the
287 various organs were measured. Sepals, petals and anthers were measured from the 15th and 16th
288 fully opened flowers on the main stem. Carpel length was measured from unfertilized flowers. Six
289 petals, six sepals, six anthers and two carpels were measured per plant. Dissected flower organs
290 were flattened and scanned at a resolution of 3200 dpi (HP ScanJet 4370). Measurements were
291 conducted on digitized images by using ImageJ [54]. Leaf size was measured on the fully expanded
292 6th leaf. The leaves were flattened and scanned at a resolution of 300 dpi using an HP ScanJet
293 4370. Measurements were then taken from the digitized images using ImageJ. [54].

294 **Morphometric analysis of petal outlines**

295 Morphometric analysis of petal shape described as closed outlines was performed using Elliptic
296 Fourier Descriptors (EFD) [55]. First, the digital images were converted into binary images using
297 ImageJ [54]. Coordinates of boundaries were extracted using the Python module scikit-image [56].
298 Outline coordinates were then analysed and visualised using the Momocs package implemented
299 in R [57].

300 **Developmental analysis of petal growth**

301 Petal cell size and cell number were determined from dried-gel agarose prints [58] of whole petals
302 from fully open flowers. Cell outlines were captured using and Olympus BX 51 light microscope
303 and AxioCam HRc camera (Carl Zeiss). The cell-outline images were merged using the
304 photomerge function of Adobe Photoshop and further processed with the Python module scikit-
305 image. First, cell-outlines were segmented using adaptive thresholding. Then, binary images of

306 cell borders were dilated, skeletonized and curated by overlapping them with the original images
307 in GIMP (https://www.gimp.org/). Cell areas and centroid coordinates were extracted and used to
308 estimate the average cell number and area per segment along the petal longitudinal axis. The
309 analysis of differences in cell number and size between genotypes was performed using R [59].
310 Curated segmented images were then analysed with ImageJ by defining Region Of Interest (ROI)
311 and measuring diverse morphological features for each particle. Heatmaps were generated in
312 ImageJ using the ROI colour coder function.

313 **Confocal imaging**

314 To visualize petal primordia, young flower buds were fixed in a solution containing 50% methanol
315 and 10% acetic acid. mPS-PI staining was carried out following the protocol by Ichihashi et al.
316 (2011)[60], with minor modifications. Imaging was performed using a confocal laser scanning
317 microscope (LSM780, Carl Zeiss), with excitation at 488 nm and emission collected between 520
318 nm and 720 nm. Z-stack images were acquired at a resolution of 512 × 512 with a step size of 0.5–
319 1 µm along the z-axis. Image stacks were processed and analyzed using MorphoGraphX [61,62].
320 Surfaces were detected using the "edge detect" tool with a threshold of 10,000. Initial meshes were
321 generated with 5 µm cubes and subsequently subdivided three times before projecting the mPS-PI
322 signal located 4-6 µm from the mesh surface.

323 **EDU staining**

324 Cell division events were visualized using a combination of 5-ethynyl-2'-deoxyuridine (EdU)
325 incorporation and modified pseudo-Schiff propidium iodide (PI; Sigma-Aldrich) staining,
326 following the protocol described in Riglet et al. (2024) with minor modifications [63]. Inflorescences
327 were harvested and placed on EdU staining medium consisting of 0.22% (w/v) Murashige and
328 Skoog basal salts with vitamins (Duchefa Biochemie, M0222.0050), 3.5% (w/v) sucrose, 0.8%
329 (w/v) agarose, and 10 µM EdU (Invitrogen A10044, Thermo Fisher Scientific), adjusted to pH 5.7.
330 Samples were submerged in the same medium lacking agarose and incubated for 15 hours in a
331 growth chamber under long-day conditions (16-hour light/8-hour dark photoperiod) at 22°C, with
332 an average light intensity of 150 µmol $m^{-2}s^{-1}$. Following incubation, samples were dehydrated
333 through a graded ethanol series (25%, 50%, 75%, 90%, and 100%; 10 minutes each), then
334 rehydrated through the same series in reverse. Tissues were then treated overnight at 37°C with 20
335 mM α-amylase (Sigma-Aldrich A4551) in phosphate buffer (pH 7.0) supplemented with 2 mM

336 NaCl and 0.25 mM $CaCl_2$. After washing twice with water and once with 100 mM Tris buffer (pH
337 8), the samples were incubated for 1 hour in a solution containing 10 μM Alexa Fluor 488-azide
338 (Invitrogen A10266) in 100 mM Tris buffer (pH 8). Subsequently, tissues were incubated for 30
339 minutes in a click-reaction solution containing 10 μM Alexa Fluor 488-azide, 100 mM Tris (pH
340 8), 1 mM $CuSO_4$, and 100 mM ascorbic acid. Samples were washed three times with water. Young
341 flower buds were dissected in water to expose petals and incubated in 1% periodic acid for 30
342 minutes, followed by two water washes. Samples were then stained with 0.01 μg μl^{-1} PI for 3
343 hours, cleared for 2 hours in chloral hydrate solution, and mounted in Hoyer's solution (30 g gum
344 arabic, 200 g chloral hydrate, 20 g glycerol, and 50 ml water). Imaging was performed using a
345 confocal laser scanning microscope (LSM780, Carl Zeiss) with excitation at 488 nm. Emission
346 was collected between 493–547 nm for EdU and 622–718 nm for PI. Z-stack images were acquired
347 at 512 × 512 resolution with a step size of 0.5–1 μm along the z-axis. EdU signals were detected
348 and quantified using ImageJ.

349 **Genetic mapping**

350 To refine the position of PAQTL_2, we conducted a segregation analysis in the *NILrg* background.
351 Initial mapping using approximately 400 progeny plants identified a 138.095 kb region on
352 chromosome 2, located between markers Bs5 (position 8,964,289) and SH3_2 (position 9,102,384)
353 (**Extended Data Table 3**). To further narrow down this interval, we screened about 1,000
354 additional progeny plants from NILrg to identify individuals with recombinant chromosomes
355 between these two markers. The positions of the recombination breakpoints were determined by
356 genotyping these recombinants with additional markers within the interval. Selfed progenies from
357 the 15 most informative recombinant lines were then genotyped to identify individuals
358 homozygous for either parental allele. Petal size was quantified in these homozygous plants, and
359 a t-test was used to compare the average petal size between genotype classes for each recombinant
360 to localize the causal mutation in relation to the position of each recombination breakpoint.
361 For fine-mapping PAQTL_2 in the *NILgo* background, we first identified a *NILgo* line segregating
362 for a ~1 Mb region surrounding PAQTL_2, located between markers JAGI (position 8,127,464)
363 and m400 (position 9,149,587) on chromosome 2 (**Extended Data Table 4**). Approximately 1,400
364 *NILgo* progeny plants were screened to identify recombinants between these markers. Each
365 recombinant was genotyped with additional markers within the focal region to pinpoint the
366 recombination breakpoints. Selected recombinant plants were selfed, and progeny were genotyped

367 to identify individuals homozygous for either the *C. grandiflora* or *C. orientalis* allele in the
368 segregating region. As described above, petal sizes of both genotype classes were measured and
369 compared using a t-test, enabling us to further refine the position of the causal mutation.

370 **Molecular cloning and plant transformation**

371 *C. rubella* (*JAGr*), *C. orientalis* (*JAGo*), two *C. grandiflora* (*JAGg1* and *JAGg2*) and two promoter
372 swap genomic constructs: *pJAGg1::JAGr* and *pJAGr::JAGg1* were used to test the existence of
373 allelic variation influencing petal size within the *JAG* locus. The 8.3 kb *JAGr*, 9.4 kb *JAGg*, 9.4
374 kb *pJAGg::JAGr* and 8.3kb *pJAGr::JAGg1* genomic constructs were amplified in two PCR
375 reactions from genomic DNA of plants homozygous for the *C. rubella* allele (*NILrr)* and plants
376 homozygous for the *C. grandiflora* allele (*NILgg1)* as described in **Extended Data Table 5**. The
377 8.3 kb *JAGo* and a 10.1 kb *JAGg2* genomic constructs were amplified in three PCR reactions from
378 genomic DNA of plants homozygous for the *C. orientalis* allele (*NILoo)* and plants homozygous
379 for the *C. grandiflora* allele (*NILgg2)* as described in **Extended Data Table 5**. Primers used are
380 presented in **Extended Data Table 6**. The genomic fragments were first assembled and subcloned
381 into a modified version of pBluescript II KS (StrataGene, pBlueMLAPUCAP) using the
382 InFusion® HD Cloning Plus kit (Clontech) and sequenced. The reconstituted cassettes were
383 transferred into the AscI site of the plant transformation vector pBarMAP, a derivative of
384 pGPTVBAR [64]. These genomic constructs were then used to transform *Crjag* and *jag-2* plants by
385 floral dip [65]. Note that since *NILrg* and *NILog* were generated from crosses with different *Cg926*
386 individuals and since *C. grandiflora* is a highly heterozygous outcrosser, the two *C. grandiflora*
387 alleles were not identical in sequence and were therefore named *JAGg1* and *JAGg2*.

388 **Identification of the *Crjag* mutation**

389 To identify the *Crjag* mutation, we followed a mapping-by-sequencing approach [66]. 500 F2
390 progeny of a cross between a mutant that we initially termed *heart-stopping (hts)* because of the
391 defect in fruit development and *Cr1504* were screened to isolate plants with a WT or mutant
392 phenotype. About 100 plants for each genotype were pooled and sequenced using the Illumina
393 NextSeq 500 instruments (2 x 100 cycles). DNA-seq data were processed using Trimmomatic [67]
394 to remove adapter sequences. Quality control was done using FastQC
395 (http://www.bioinformatics.bbsrc.ac.uk/projects/fastqc). Reads were then mapped at per sample
396 level against the *C.rubella* reference genome (Cru_183 from phytozome.org) using BWA-MEM

397 [68]. Variant calling was performed using SAMtools [69]. Those calls were then further processed using
398 R [59] to extract *Cr22.5* (background of *crjag* mutation)/*Cr1504* polymorphisms. The ratio between
399 the number of homozygous and heterozygous calls within 200 kb windows was used to localize
400 the mutation.

401 **RNA splicing analysis**

402 To detect splicing differences, RNA was first extracted from *Crjag* and *Cr22.5* inflorescences
403 (containing the inflorescence meristem and the flower buds from stage 1 to 9) using Trizol (Life
404 Technologies). RNAs were treated with TurboDNAse (Ambion) and reverse transcribed using
405 oligo(dT) and the Superscript III Reverse Transcriptase (Invitrogen). Primers onw545 and onw546
406 were used to amplify full-length *JAG* transcripts.

407 **Modelling of petal growth**

408 The *Capsella* petal growth model is based on a 2D Arabidopsis thaliana petal growth model
409 developed by Susanna Sauret-Güeto *et al.*, 2013 [45]. Models were specified and manipulated using
410 the MATLAB-based application *GFTbox* [70]. Growth patterns are guided by spatially distributed
411 factors across a tissue framework, referred to as the canvas. In this model, the initial canvas
412 consists of approximately 2,300 elements and measures 30 µm in both width and length. Each
413 factor is assigned a value at either the segments or vertices of the canvas, where it promotes growth
414 rates through a linear function (**Extended Data Fig. 8**). The model integrates two interconnected
415 regulatory networks:

416 - The Polarity Regulatory Network (PRN), which defines tissue polarity and orients growth
417 along the canvas.
418 - The Growth Rate Regulatory Network (GRRN), which modulates the local growth rates.

419 Polarity is established by the propagation of the factor POL, from a proximal organizer
420 (PROXORG) toward a distal organizer called DISTORG. In the most realistic divergent model,
421 DISTORG is expressed at the distal petal margin where it consumes POL, creating a divergence
422 in the polarity field. This causes the growth direction to shift away from the petal midline and
423 toward the margins in the distal region. Another key factor, DISGRAD, is predominantly
424 expressed in the distal region, where it promotes growth perpendicular to the mid-petal axis (Kpar,
425 or Kper). This model successfully replicates *Arabidopsis thaliana* petal development and is

426 supported by molecular data, which, in accordance with our observations, suggest that *JAG*
427 functions as a distal factor DGRAD and that auxin biosynthesis and signaling are involved in the
428 establishment of the polarity field. Although this model accurately simulates *A. thaliana* petal
429 growth, it fails to reproduce the petal shape of *Capsella* species, despite very similar overall growth
430 rates (**Extended Data Fig. 9**). In *C. grandiflora*, petal growth dynamics are similar to those of *A.*
431 *thaliana*, but the length-to-width ratio is significantly lower. Simply increasing Kper with the basic
432 growth parameter did not generate realistic *Cg* petal shapes, as it only widened the distal region,
433 maintaining a lobed shape, whereas *Cg* petals are generally more rounded. More realistic outlines
434 were obtained by expanding both the DISTORG and DGRAD domains.
435 However, reducing DGRAD activity in this modified model did not significantly decrease petal
436 length, as observed in *crjag* mutants (**Fig. 3**). To address this discrepancy, we modified the model
437 so that DGRAD also affected Kpar, which resulted in petals highly similar in shape and size to
438 those of *Cg*. Furthermore, abolishing DGRAD activity while accounting for the fragmented distal
439 auxin distribution in *jag* petals (as in [45]) led to a significant decrease in petal length, resulting in
440 'jagged' petals approximately 1.5 mm long, closely resembling *crjag* mutants. The models are
441 provided as supplemental dataset and the parameters of the models used are presented in **Extended**
442 **Data Table 7**.
443 Leaf growth was modeled using the organizer-based fixed polarity model described by Kuchen et
444 al. (2012) [46]. In this model, tissue polarity is established by diffusion of a polarity factor (POL)
445 from a proximal organiser (PROXORG) at the base of the canvas. After an initial equilibration
446 phase, the POL gradient is fixed and deforms passively with the tissue during growth. Growth
447 parallel to the polarity field is promoted by PGRAD, while LAM promotes growth perpendicular
448 to the polarity. MID inhibits perpendicular growth along the midline, and LATE modulates both
449 parallel and perpendicular growth. All growth regulators remain fixed to their initial spatial
450 distributions throughout development. Because crjag mutant leaves exhibit a 14% reduction in
451 length and an 18% reduction in width, we assumed that JAG contributes similarly to both PGRAD
452 and LAM activity. The model was therefore calibrated to reproduce the phenotypic differences
453 observed in crjag leaves. We then ran both the petal and leaf models for the same number of
454 iterations while varying the level of *JAG* activity according to its overall contribution to organ
455 growth.

456 **Population genetics**

457 We focused our analysis on polymorphisms segregating between the genotypes used for transgenic
458 analysis, since they carry the alleles responsible for variation in petal size between mating
459 strategies. Multiple sequence alignment of the four accessions' JAG sequences (*C. rubella*, *C.*
460 *grandiflora Cg1* and *Cg2*, and *C. orientalis*) was performed using MAFFT. Polymorphisms were
461 identified from this alignment, which was then used to generate a consensus JAG sequence
462 including all indels and the most frequent allele at each polymorphic site, using EMBOSS cons
463 (parameters: -setcase 0 -plurality 1). This consensus sequence replaced the native *JAG* sequence
464 from the *C. rubella* reference genome (version 183).
465 We used this custom reference for read mapping of publicly available resequencing datasets
466 (GATK pipeline), including 180 *C. grandiflora* individuals from a single population, 51 *C. rubella*,
467 and 16 *C. orientalis* [71–73]. The resulting VCF file contained 3,300 polymorphisms in the *JAG*
468 coding and cis-regulatory regions. Indels were normalized using bcftools (norm followed by filter
469 --IndelGap 5), applying parsimony and left-alignment, which reduced the set to 2,371
470 polymorphisms. We further curated the VCF applying the following filters: (i) remove
471 polymorphisms located within large indels based on haplotypes used in transgenic experiments
472 (accounted for ~75% of the polymorphisms) (ii) remove polymorphisms absent from the
473 genotypes used for introgression and complementation experiments; (iii) simplify indel
474 annotations not fully resolved during normalization; and (iv) inspect ambiguous sites using IGV
475 to resolve ambiguous or missing information. After filtering, the final dataset contained 340
476 polymorphisms for the Cg-Cr comparison and 536 for the Cg–Co comparison, among which 164
477 were shared. Among the 164 shared polymorphisms, i.e. the major allele in *Cg* differs from the
478 major allele of *Cr* and *Co*, 84 were called convergent, i.e. the fixed allele in Cg (frequency >75%)
479 differs from the fixed allele in Cr and Co (frequency >90%).
480 To facilitate downstream association analyses, multiallelic sites in the VCF were decomposed into
481 biallelic pseudo-loci. For each multiallelic site, the list of alternative (ALT) alleles was extracted,
482 and each ALT allele was treated as a separate locus. Genotypes were recoded as allele counts (0,
483 1, or 2 copies of the ALT allele), with missing data set to NA. This procedure was applied to all
484 variants, and the resulting expanded genotype matrix was used for downstream analyses.

485 **Phenotypic association analysis and detection of overdominance**

486 Phenotypic measurements for *Cg* individuals with available genomic information were retrieved
487 from [26] and filtered to remove individuals with missing values. Genotypic data were converted into
488 an individual-by-locus matrix, coded numerically, and merged with the phenotypic dataset. For
489 each trait–locus combination, we tested for overall genotype effects using linear models with the
490 genotype as a categorical predictor. Loci with fewer than 10 individuals in any genotype class were
491 excluded from analysis. The overall significance of genotype effects was assessed by ANOVA,
492 and per-term p-values were adjusted for multiple testing using the Benjamini–Hochberg false
493 discovery rate (FDR) procedure.
494 To formally test for overdominance, we applied an additive–dominance model in which
495 heterozygotes were explicitly coded as a binary variable. For each locus–trait pair with adequate
496 sample size in all three genotype classes, we fitted the model Phenotype ~ additive + dominance
497 and identified significant dominance effects ($p < 0.05$) where heterozygotes exceeded both
498 homozygotes in mean phenotype. Overdominant candidates were defined as loci that (i) showed a
499 significant dominance term, and (ii) had heterozygous mean phenotypes greater than both
500 homozygotes in the filtered dataset. Overlap between these statistical and phenotypic criteria was
501 used to generate the final list of overdominant loci. Candidate loci were annotated with SNP
502 metadata and visualized using boxplots and Manhattan-like genome position plots, with
503 overdominant loci highlighted. The list of phenotype based overdominant polymorphisms was
504 compared to the list of convergent polymorphisms.

505 **Identification of overdominant loci through inbreeding coefficient**

506 Observed genotype counts per locus (nAA, nAB, nBB) were calculated from the expanded
507 genotype matrix. From these, observed heterozygosity (H_o), expected heterozygosity (H_e), and the
508 inbreeding coefficient ($F_{IS} = 1 - H_o/H_e$) were computed. Hardy–Weinberg equilibrium (HWE)
509 exact tests were performed using the HardyWeinberg package in R. Loci were classified as
510 overdominant if they satisfied all of the following criteria: (i) significant deviation from HWE (p
511 < 0.05), (ii) negative F_{IS} values (heterozygote excess), and (iii) $H_o > H_e$. Chromosome-wise plots
512 of F_{IS} against genomic position were generated, marking overdominant loci and convergent
513 overdominant (based on phenotype) candidates.

514 **Simulation of the influence of overdominant selection on allele trajectories**

515 We conducted a common garden experiment at the University of Potsdam, Germany, using an F_2
516 population derived from a cross between *Cg* and *Cr*. Plants homozygous for the *Cg* (functional)
517 allele at the self-incompatibility locus were selected, and their petal size was quantified.
518 Reproductive efficiency was estimated as the number of seeds produced per fruit (which reflects
519 animal pollination), normalised by the average number of ovules developed by each individual
520 and used as a proxy for pollination-mediated female fitness.
521 The relationship between petal size and reproductive efficiency was assessed using Pearson's
522 correlation. A linear regression model was then fitted with reproductive efficiency as the response
523 variable and petal area as the predictor. Regression coefficients and R^2 values were extracted to
524 describe the strength and direction of the relationship. For visualization, scatterplots with fitted
525 regression lines and annotated regression equations were generated.
526 Allele frequency dynamics were simulated using a discrete-generation Wright–Fisher model. The
527 model incorporated: Effective population size N_e =500,000, 10^6 generations and an initial allele
528 frequency p_0 =0.1 and selection gradient derived from genotype-phenotype relationships. For each
529 replicate (500 replicates), genotype frequencies were adjusted according to selection coefficients,
530 and the next generation was sampled multinomially to account for genetic drift. Simulations were
531 also conducted under neutrality (no selection) for comparison.
532 Fitness of genotypes was modelled linearly as a function of deviation from the mean phenotypic
533 value:

534 $$wi = 1 + \beta(Gi - \bar{G})$$

535 where β is the selection coefficient relating phenotype to fitness, *Gi* is the genotype's phenotypic
536 value, and $\bar{G}$ is the population mean. Overdominance was assessed by comparing heterozygote
537 fitness to the two homozygotes. A stable internal equilibrium allele frequency $\hat{p}$ was estimated
538 when overdominance was detected.
539 For each simulation replicate, we recorded allele frequencies across generations and at the final
540 generation: homozygote and heterozygote counts, observed heterozygosity (*Ho*), expected
541 heterozygosity (*He*), and *Fis*. Hardy–Weinberg equilibrium was tested using exact tests, and the
542 proportion of replicates deviating from equilibrium at α=0.05 was reported.
543 Allele frequency trajectories were summarized as mean ± 95% confidence intervals across
544 replicates. Final-generation allele frequencies were visualized as histograms, and probabilities of

maintaining polymorphism were estimated as the proportion of replicates with 0 < heterozygote frequency < 1.

Statistical analyses

Statistical analyses were performed using R (version 4.2.1). Two-tailed Student's t-test assuming unequal variances was used for two-sample comparisons. For multiple comparisons, we conducted Tukey's HSD tests, performed using the R/agricolae package. Data visualization was done using the R/ggplot2 package or R/base. In all boxplots, the middle lines represent the median, the lower and upper hinges correspond to the first and third quartile, respectively. The upper and lower whiskers add or subtract 1.5 interquartile ranges to/from the 75 and 25 percentile, respectively. Overdomiance was tested using Linear mixed-effects models,fitted using the lmer function in the lme4 package. Estimated marginal means were obtained using the emmeans package. Planned contrasts between genotypes were tested with Bonferroni-adjusted p-values, and degrees of freedom were approximated using the Kenward-Roger method.

Data availability:

The genome sequence data used in this manuscript have been previous deposited to NCBI's Sequence Read Archive (SRA) or the European Nucleotide Archive (ENA) under the accession number SRA: PRJNA1233196, PRJNA1233196, PRJNA275635 and PRJEB6689 and are publicly available. All materials used in this study are available upon request.

References

1. Stern, D. L. The genetic causes of convergent evolution. *Nat. Rev. Genet.* **14**, 751–64 (2013).
2. Blount, Z. D., Lenski, R. E. & Losos, J. B. Contingency and determinism in evolution: Replaying life's tape. *Science (80-.).* **362**, (2018).
3. Hether, T. D. & Hohenlohe, P. A. GENETIC REGULATORY NETWORK MOTIFS CONSTRAIN ADAPTATION THROUGH CURVATURE IN THE LANDSCAPE OF MUTATIONAL (CO)VARIANCE. *Evolution (N. Y).* **68**, 950–964 (2014).
4. Stephen Jay Gould. *Wonderful Life: The Burgess Shale and the Nature of History*. (W.W. Norton & Company, 1989).
5. Hoitinga, P. K. & Birkeland, S. Pathway-level convergence: an underexplored aspect of convergent evolution. *Trends Genet.* https://doi.org/10.1016/j.tig.2025.06.009 (2025) doi:10.1016/j.tig.2025.06.009.
6. Tsuchimatsu, T. & Fujii, S. The selfing syndrome and beyond: diverse evolutionary consequences of mating

577 system transitions in plants. *Philos. Trans. R. Soc. B Biol. Sci.* **377**, (2022).
578 7. Shimizu, K. K. & Tsuchimatsu, T. Evolution of Selfing: Recurrent Patterns in Molecular Adaptation. *Annu.*
579 *Rev. Ecol. Evol. Syst.* **46**, 112414–054249 (2015).
580 8. Wright, S. I., Ness, R. W., Foxe, J. P. & Barrett, S. C. H. Genomic Consequences of Outcrossing and
581 Selfing in Plants. *Int. J. Plant Sci.* **169**, 105–118 (2008).
582 9. Cruden, R. Pollen-Ovule Ratios: A Conservative Indicator of Breeding Systems in Flowering Plants
583 Evolution. *Biol. J. Linn. Soc.* 32–46 (1977).
584 10. Barrett, S. C. H. The evolution of plant sexual diversity. *Nat. Rev. Genet.* **3**, 274–84 (2002).
585 11. Blarer, A., Keasar, T. & Shmida, A. Possible mechanisms for the formation of flower size preferences by
586 foraging bumblebees. *Ethology* https://doi.org/10.1046/j.1439-0310.2002.00778.x (2002)
587 doi:10.1046/j.1439-0310.2002.00778.x.
588 12. Fenster, C. B., Cheely, G., Dudash, M. R. & Reynolds, R. J. Nectar reward and advertisement in
589 hummingbird-pollinated Silene virginica (Caryophyllaceae). *Am. J. Bot.*
590 https://doi.org/10.3732/ajb.93.12.1800 (2006) doi:10.3732/ajb.93.12.1800.
591 13. Goodwillie, C. *et al.* Correlated evolution of mating system and floral display traits in flowering plants and
592 its implications for the distribution of mating system variation. *New Phytol.* **185**, 311–321 (2010).
593 14. Sicard, A. & Lenhard, M. The selfing syndrome: a model for studying the genetic and evolutionary basis of
594 morphological adaptation in plants. *Ann. Bot.* **107**, 1433–1443 (2011).
595 15. Frary, A., Fritz, L. A. & Tanksley, S. D. A comparative study of the genetic bases of natural variation in
596 tomato leaf, sepal, and petal morphology. *Theor. Appl. Genet.* https://doi.org/10.1007/s00122-004-1669-x
597 (2004) doi:10.1007/s00122-004-1669-x.
598 16. Slotte, T., Hazzouri, K. M., Stern, D., Andolfatto, P. & Wright, S. I. Genetic architecture and adaptive
599 significance of the selfing syndrome in Capsella. *Evolution* **66**, 1360–74 (2012).
600 17. Sicard, A. *et al.* Genetics, evolution, and adaptive significance of the selfing syndrome in the genus
601 Capsella. *Plant Cell* **23**, 3156–71 (2011).
602 18. Fishman, L., Kelly, A. J. & Willis, J. H. Minor quantitative trait loci underlie floral traits associated with
603 mating system divergence in Mimulus. *Evolution (N. Y).* **56**, 2138–2155 (2002).
604 19. Fishman, L., Beardsley, P. M., Stathos, A., Williams, C. F. & Hill, J. P. The genetic architecture of traits
605 associated with the evolution of self-pollination in Mimulus. *New Phytol.* https://doi.org/10.1111/nph.13091
606 (2015) doi:10.1111/nph.13091.
607 20. Lin, J. Z. & Ritland, K. Quantitative trait loci differentiating the outbreeding Mimulus guttatus from the
608 inbreeding M. platycalyx. *Genetics* **146**, 1115–1121 (1997).
609 21. Goodwillie, C., Ritland, C. & Ritland, K. The genetic basis of floral traits associated with mating system
610 evolution in Leptosiphon (Polemoniaceae): an analysis of quantitative trait loci. *Evolution* **60**, 491–504
611 (2006).
612 22. Georgiady, M. S., Whitkus, R. W. & Lord, E. M. Genetic analysis of traits distinguishing outcrossing and
613 self-pollinating forms of currant tomato, Lycopersicon pimpinellifolium (Jusl.) Mill. *Genetics* **161**, 333–344
614 (2002).

615 23. Grillo, M. A. *et al.* Genetic architecture for the adaptive origin of annual wild rice, Oryza nivara. *Evolution*
616 *(N. Y).* https://doi.org/10.1111/j.1558-5646.2008.00602.x (2009) doi:10.1111/j.1558-5646.2008.00602.x.
617 24. Stern, D. L. & Orgogozo, V. The loci of evolution: how predictable is genetic evolution? *Evolution* **62**,
618 2155–77 (2008).
619 25. Dittmar, E. L., Oakley, C. G., Conner, J. K., Gould, B. A. & Schemske, D. W. Factors influencing the effect
620 size distribution of adaptive substitutions. *Proc. R. Soc. B Biol. Sci.* **283**, 20153065 (2016).
621 26. Sicard, A. *et al.* Standing genetic variation in a tissue-specific enhancer underlies selfing-syndrome
622 evolution in Capsella. *Proc. Natl. Acad. Sci.* **113**, 13911–13916 (2016).
623 27. Slotte, T., Hazzouri, K. M., Stern, D., Andolfatto, P. & Wright, S. I. Genetic architecture and adaptive
624 significance of the selfing syndrome in Capsella. *Evolution* **66**, 1360–74 (2012).
625 28. Slotte, T. *et al.* The Capsella rubella genome and the genomic consequences of rapid mating system
626 evolution. *Nat. Genet.* **45**, 831–5 (2013).
627 29. Jantzen, F. *et al.* Retracing the molecular basis and evolutionary history of the loss of benzaldehyde
628 emission in the genus Capsella. *New Phytol.* **224**, 1349–1360 (2019).
629 30. Sas, C. *et al.* Repeated Inactivation of the First Committed Enzyme Underlies the Loss of Benzaldehyde
630 Emission after the Selfing Transition in Capsella Report Repeated Inactivation of the First Committed
631 Enzyme Underlies the Loss of Benzaldehyde Emission after the Selfi. 3313–3319 (2016)
632 doi:10.1016/j.cub.2016.10.026.
633 31. Wozniak, N. J. *et al.* A Similar Genetic Architecture Underlies the Convergent Evolution of the Selfing
634 Syndrome in Capsella. *Plant Cell* **32**, tpc.00551.2019 (2020).
635 32. Woźniak, N. J. *et al.* Convergence and molecular evolution of floral fragrance after independent transitions
636 to self-fertilization. *Curr. Biol.* **34**, 2702-2711.e6 (2024).
637 33. Fujikura, U. *et al.* Variation in Splicing Efficiency Underlies Morphological Evolution in Capsella. *Dev.*
638 *Cell* **44**, 192-203.e5 (2017).
639 34. Brandvain, Y., Slotte, T., Hazzouri, K. M., Wright, S. I. & Coop, G. Genomic Identification of Founding
640 Haplotypes Reveals the History of the Selfing Species Capsella rubella. *PLoS Genet.* **9**, e1003754 (2013).
641 35. Bachmann, J. A. *et al.* Genetic basis and timing of a major mating system shift in Capsella. *bioRxiv*
642 https://doi.org/10.1101/425389 (2018) doi:10.1101/425389.
643 36. Hurka, H., Friesen, N., German, D. A., Franzke, A. & Neuffer, B. 'Missing link' species Capsella orientalis
644 and Capsella thracica elucidate evolution of model plant genus Capsella (Brassicaceae). *Mol. Ecol.*
645 https://doi.org/10.1111/j.1365-294X.2012.05460.x (2012) doi:10.1111/j.1365-294X.2012.05460.x.
646 37. Wozniak, N., Kappel, C., Marona, C. Altschmied, L., Neuffer B., Sicard, A. *Chapter 2 : A Common*
647 *Molecular Basis to the Convergent Evolution of the Selfing Syndrome in Capsella*.
648 38. Woźniak, N. J. *et al.* A Similar Genetic Architecture Underlies the Convergent Evolution of the Selfing
649 Syndrome in Capsella. *Plant Cell* **32**, 935–949 (2020).
650 39. Sicard, A. *et al.* Genetics, evolution, and adaptive significance of the selfing syndrome in the genus
651 Capsella. *Plant Cell* **23**, 3156–3171 (2011).
652 40. Ohno, C. K. The Arabidopsis JAGGED gene encodes a zinc finger protein that promotes leaf tissue

development. *Development* https://doi.org/10.1242/dev.00991 (2004) doi:10.1242/dev.00991.

41. Turner, T. L. Fine-mapping natural alleles: quantitative complementation to the rescue. *Mol. Ecol.* **23**, 2377–2382 (2014).

42. Dong, Y. *et al.* Epigenetic regulation of fruit shape determination by JAGGED gene in Capsella rubella. at https://doi.org/10.21203/rs.3.rs-8265099/v1 (2026).

43. Sauret-Güeto, S., Schiessl, K., Bangham, A., Sablowski, R. & Coen, E. JAGGED Controls Arabidopsis Petal Growth and Shape by Interacting with a Divergent Polarity Field. *PLoS Biol.* **11**, (2013).

44. Schiessl, K., Muiño, J. M. & Sablowski, R. Arabidopsis JAGGED links floral organ patterning to tissue growth by repressing Kip-related cell cycle inhibitors. *Proc. Natl. Acad. Sci.* **111**, 2830–2835 (2014).

45. Sauret-Güeto, S., Schiessl, K., Bangham, A., Sablowski, R. & Coen, E. JAGGED Controls Arabidopsis Petal Growth and Shape by Interacting with a Divergent Polarity Field. *PLoS Biol.* **11**, e1001550 (2013).

46. Kuchen, E. E. *et al.* Generation of Leaf Shape Through Early Patterns of Growth and Tissue Polarity. *Science (80-.).* **335**, 1092–1096 (2012).

47. Dinneny, J. R. The role of JAGGED in shaping lateral organs. *Development* **131**, 1101–1110 (2004).

48. He, X. *et al.* JAG modulates sepal flatness by regulating cell growth direction, interacts with AS2, and is antagonized by TCP24. *Cell Rep.* **44**, 115950 (2025).

49. Hurka, H., Friesen, N., German, D. a, Franzke, A. & Neuffer, B. 'Missing link' species Capsella orientalis and Capsella thracica elucidate evolution of model plant genus Capsella (Brassicaceae). *Mol. Ecol.* **21**, 1223–38 (2012).

50. Bachmann, J. A. *et al.* Genetic basis and timing of a major mating system shift in Capsella. *New Phytol.* **224**, 505–517 (2019).

51. Foxe, J. P. *et al.* Recent speciation associated with the evolution of selfing in Capsella. *Proc. Natl. Acad. Sci. U. S. A.* **106**, 5241–5 (2009).

52. Lachance, J. Detecting selection-induced departures from Hardy-Weinberg proportions. *Genet. Sel. Evol.* **41**, 15 (2009).

53. Streubel, S., Fritz, M. A., Teltow, M., Kappel, C. & Sicard, A. Successive duplication-divergence mechanisms at the RCO locus contributed to leaf shape diversity in the Brassicaceae. *Development* (2018).

54. Abramoff, M. D., Magalhaes, P. J. & Ram, S. J. ImageJ. *Biophotonics Int.* https://doi.org/DOI: 10.1016/S0022-3115(02)01073-5 (2004) doi:DOI: 10.1016/S0022-3115(02)01073-5.

55. Kuhl, F. P. & Giardina, C. R. Elliptic Fourier features of a closed contour. *Comput. Graph. image Process.* **18**, 236–258 (1982).

56. van der Walt, S. *et al.* scikit-image: image processing in Python. *PeerJ* **2**, e453 (2014).

57. Claude, J. *Morphometrics with RNo Title*. (Springer-Verlag New York, 2008). doi:10.1007/978-0-387-77789-4.

58. Horiguchi, G., Fujikura, U., Ferjani, A., Ishikawa, N. & Tsukaya, H. Large-scale histological analysis of leaf mutants using two simple leaf observation methods: Identification of novel genetic pathways governing the size and shape of leaves. *Plant J.* **48**, 638–644 (2006).

691 59. R Core Team. R: A language and environment for statistical computing. *R Found. Stat. Comput. Vienna,*
692 *Austria.* (2018).
693 60. Ichihashi, Y. *et al.* Key Proliferative Activity in the Junction between the Leaf Blade and Leaf Petiole of
694 Arabidopsis. *Plant Physiol.* **157**, 1151–1162 (2011).
695 61. Barbier de Reuille, P. *et al.* MorphoGraphX: A platform for quantifying morphogenesis in 4D. *Elife* **4**, 1–20
696 (2015).
697 62. Strauss, S. *et al.* Using positional information to provide context for biological image analysis with
698 MorphoGraphX 2.0. *Elife* **11**, (2022).
699 63. Riglet, L. *et al.* Hibiscus bullseyes reveal mechanisms controlling petal pattern proportions that influence
700 plant-pollinator interactions. *Sci. Adv.* **10**, (2024).
701 64. Becker, D., Kemper, E., Schell, J. & Masterson, R. New plant binary vectors with selectable markers located
702 proximal to the left T-DNA border. *Plant Mol. Biol.* **20**, 1195–1197 (1992).
703 65. Clough, S. J. & Bent, A. F. Floral dip: A simplified method for Agrobacterium-mediated transformation of
704 Arabidopsis thaliana. *Plant J.* https://doi.org/10.1046/j.1365-313X.1998.00343.x (1998) doi:10.1046/j.1365-
705 313X.1998.00343.x.
706 66. James, G. V. *et al.* User guide for mapping-by-sequencing in Arabidopsis. *Genome Biol.*
707 https://doi.org/10.1186/gb-2013-14-6-r61 (2013) doi:10.1186/gb-2013-14-6-r61.
708 67. Bolger, A. M., Lohse, M. & Usadel, B. Trimmomatic: A flexible trimmer for Illumina sequence data.
709 *Bioinformatics* **30**, 2114–2120 (2014).
710 68. Li, H. Aligning sequence reads, clone sequences and assembly contigs with BWA-MEM. *arXiv Prepr. arXiv*
711 **00**, 3 (2013).
712 69. Li, H. *et al.* The Sequence Alignment/Map format and SAMtools. *Bioinformatics* **25**, 2078–9 (2009).
713 70. Kennaway, R., Coen, E., Green, A. & Bangham, A. Generation of Diverse Biological Forms through
714 Combinatorial Interactions between Tissue Polarity and Growth. *PLoS Comput. Biol.* **7**, e1002071 (2011).
715 71. Agren, J. A. *et al.* Mating system shifts and transposable element evolution in the plant genus Capsella.
716 *BMC Genomics* **15**, 602 (2014).
717 72. Koenig, D. *et al.* Long-term balancing selection drives evolution of immunity genes in capsella. *Elife* **8**, 1–
718 27 (2019).
719 73. Josephs, E. B., Lee, Y. W., Stinchcombe, J. R. & Wright, S. I. Association mapping reveals the role of
720 purifying selection in the maintenance of genomic variation in gene expression. *Proc. Natl. Acad. Sci. U. S.*
721 *A.* **112**, 15390–15395 (2015).
722

723 **Acknowledgments**

724 We thank Fredric Hedlund and Kathrin Hesse for plant care and members of the Lenhard and Rosa
725 groups for discussion and comments on the article. The computation and data handling were
726 provided by the Swedish National Infrastructure for Computing (SNIC) at Uppmax, partially
727 funded by the Swedish Research Council through grant agreement no 2018-05973. This work was

supported by: Deutsche Forschungsgemeinschaft grant SI1967/2 (AS) Swedish Research Council grant 2018-04214 (AS, KS) and theNovo Nordisk Fonden NNF22OC0079830 (AS, KS)

Author contributions

K.S., N.W. and A.P. performed and analysed the experiments. U.F. generated transgenic lines, and T.F.L. contributed to phenotypic analyses of mutant lines. C.K. carried out the bioinformatic analyses. A.S. acquired funding, administered the project and, together with M.L., S.R. and Y.D., supervised the research. A.S., N.W., K.S. and A.P. drafted the manuscript, and all authors contributed to revising and editing the final version.

Ethics declarations

Competing interests

The authors declare no competing interests.

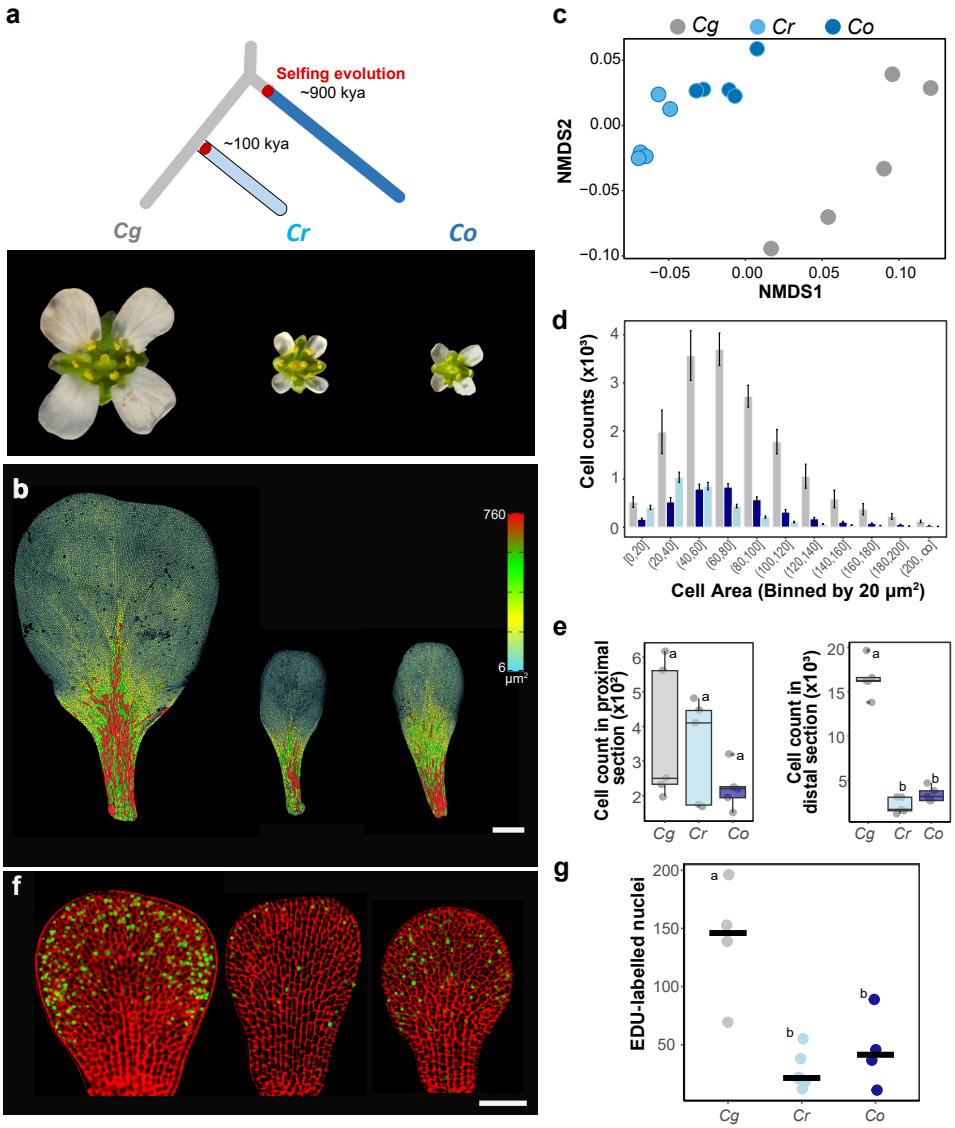

Fig. 1: Convergent evolution of petal size following the transition to selfing in *Capsella*.

a, Schematic representation of the evolutionary history within the *Capsella* genus. **b,** Heatmap illustrating the distribution of cell size within the petals of the three *Capsella* species. Scale bar: 400 µm. **c,** Non-metric multidimensional scaling (NMDS) plot based on Bray-Curtis dissimilarities in cellular features among *C. grandiflora*, *C. rubella*, and *C. orientalis* petals (n = 5 per species). **d,** Average cell count per cell area bin (n = 5 per species). **e,** Cell counts within the proximal and distal regions of the petals. **f,** Representative images showing the distribution of cell division events across the epidermis of stage 1 petals. Fluorescently labelled nucleotide analogue 5-ethynyl-2'-deoxyuridine (EdU; green) was used to visualise newly synthesised DNA, and primary cell walls were stained with propidium iodide (PI; red). Scale bar: 50 µm. **g,** Quantification of EdU-labelled nuclei in stage 1 petals. Letters indicate significant differences as determined by one-way ANOVA with Tukey's HSD test (α = 0.05).

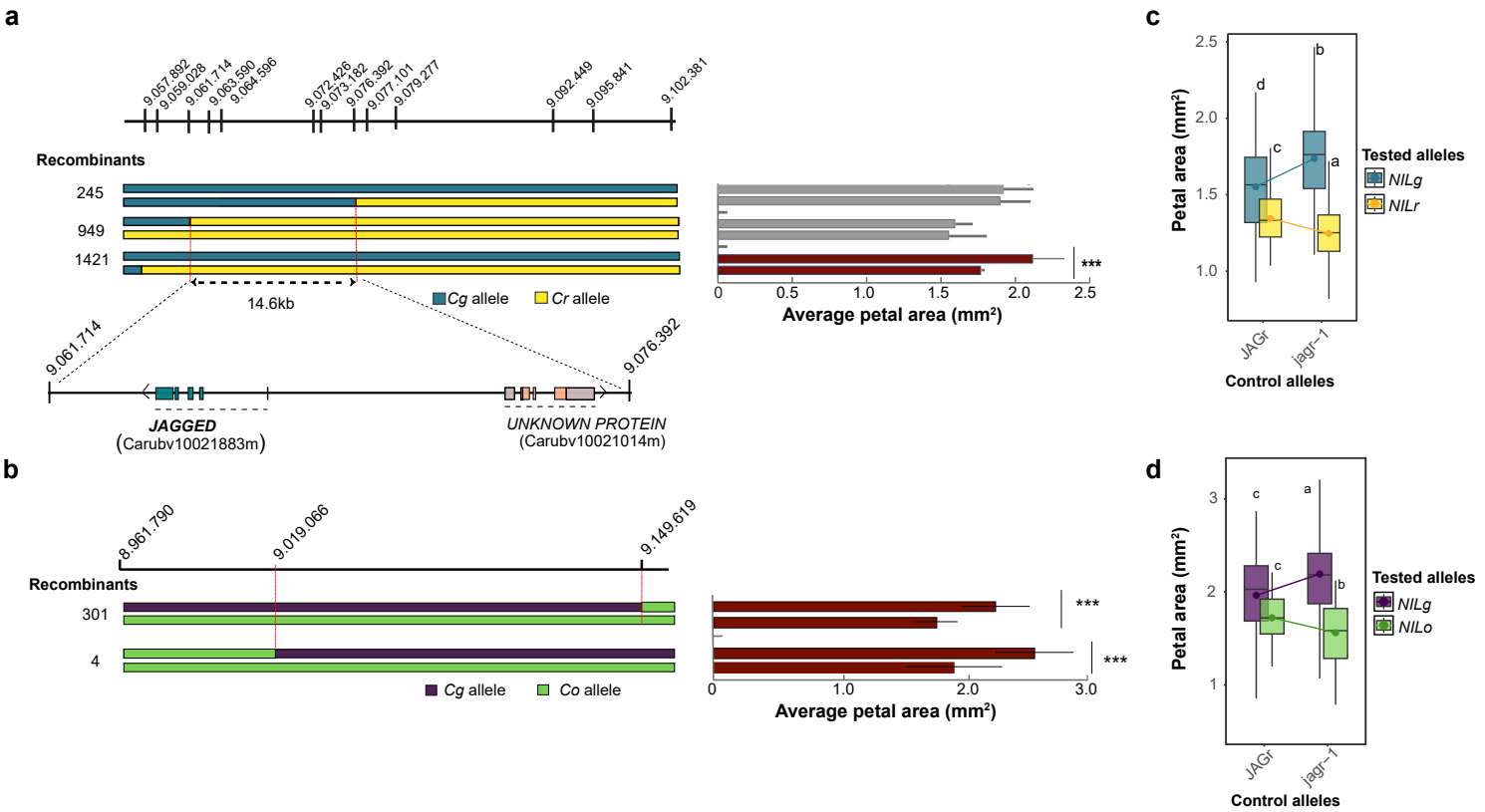

Fig. 2. Allelic variation within *JAG* contribute to petal size reduction in indepdent selfing lineages.
a and **b** Fine mapping of PA_QTL2 in *C. rubella* (*Cr*) and *C.orientalis (Co)*, respectively. The color coded bars on the left repsent the genotype of the most informative recombinants. The position on scaffold 2 are indicated on the top in base pair (bp). The bar chart on the right shows the average petal size for each alternative homozygous plants for each recombinant lines. Red filled bars indicate significant differences between alternative homozygous genotypes, P <0.05 (Student's t-test). **c** and **d** Quantitative complementation assay illustrated with an interaction plot of the crosses between *NILrg* **c** or *NILog* **d** with *jagr-1*+/-. Letters indicate significant differences as determined by one-way ANOVA with Tukey's HSD test (α = 0.05).

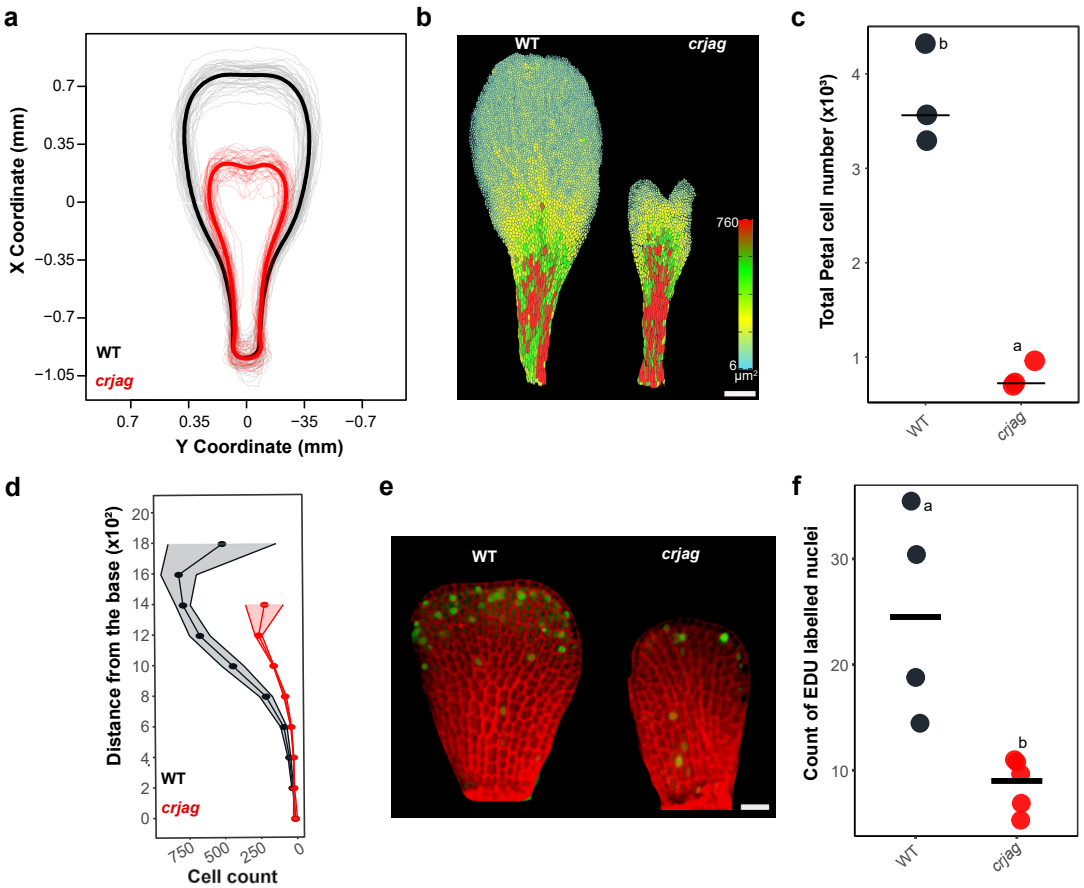

Fig. 3. Loss of *JAG* function strongly inhibits cell proliferation during petal growth.

a, Average shape of *Cr* and *crjag* petals. **b,** Heatmap illustrating the distribution of cell size within the petals of *Cr* and *crjag*. Scale bar: 200 µm. **c,** Total number of cell within *Cr* and *crjag* petals (n = 3 per genotype). **d,** Average cell count per 200 µm section along the longitudinal petal axis (n = 3 per genotype). Numbers on the y-axis indicate the starting point of each section. **e,** Representative images showing the distribution of cell division events across the epidermis of stage 1 petals. Fluorescently labelled nucleotide analogue 5-ethynyl-2'-deoxyuridine (EdU; green) was used to visualize newly synthesized DNA, and primary cell walls were stained with propidium iodide (PI; red). Scale bar: 20 µm. **f,** Quantification of EdU-labelled nuclei in stage 1 petals. Letters indicate significant differences as determined by one-way ANOVA with Tukey's HSD test ($\alpha = 0.05$).

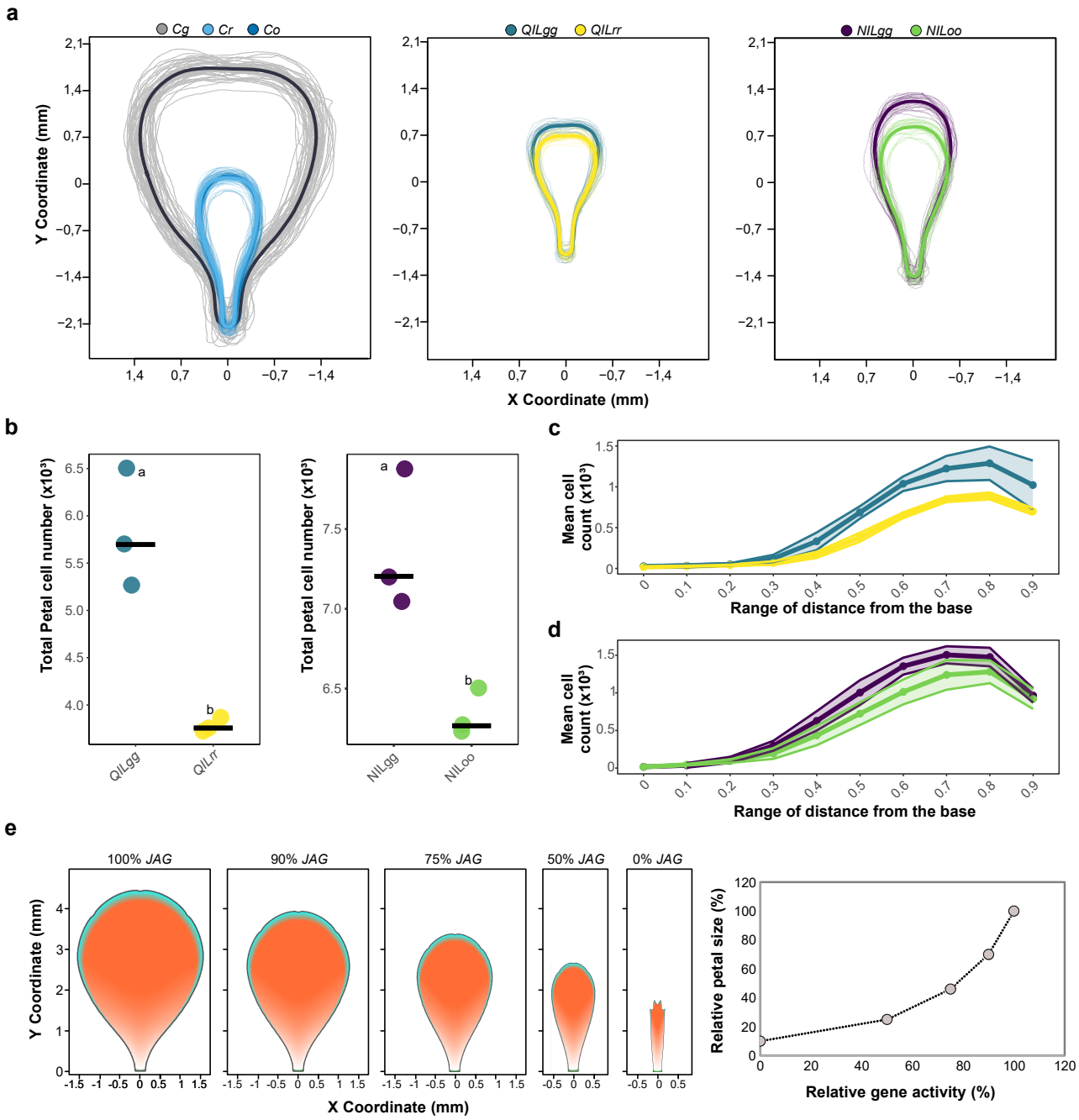

Fig. 4. Developmental constraint on petal size evolution via heightened *JAG* sensitivity.
a, Average petal shape of *Cg*, *Cr* and *Co* petals (left panel), of quasi Isogenic lines (*QIL*) homozygous for the *Cg1JAG* (QILgg) or *CrJAG* (QILrr) allele (middle panel) and of Near Isogenic lines (*QIL*) homozygous for the *Cg2JAG* (*NILLgg*) or *CoJAG* (*NILLoo*) allele (right panel). **b,** Total number of cell within *QILgg* and *QILrr* and within *NILgg* and *NILoo* petals (n = 3 per genotype). **c-d**, Average cell count for 10 section along the longitudinal axis within *QILgg* and *QILrr* (**c**) and within *NILgg* and *NILoo* (**d**) petals (n = 3 per genotype). Numbers on the y-axis indicate the starting point of each section. **e,** Output of the *Capsella* petal development model with a divergent polarity field. The effect of *JAG* on basic growth parameters was progressively reduced, as indicated at the top of each graph from left to right. The rightmost graph shows the impact of decreased *JAG* activity on petal size. Letters indicate significant differences as determined by one-way ANOVA with Tukey's HSD test (α = 0.05).

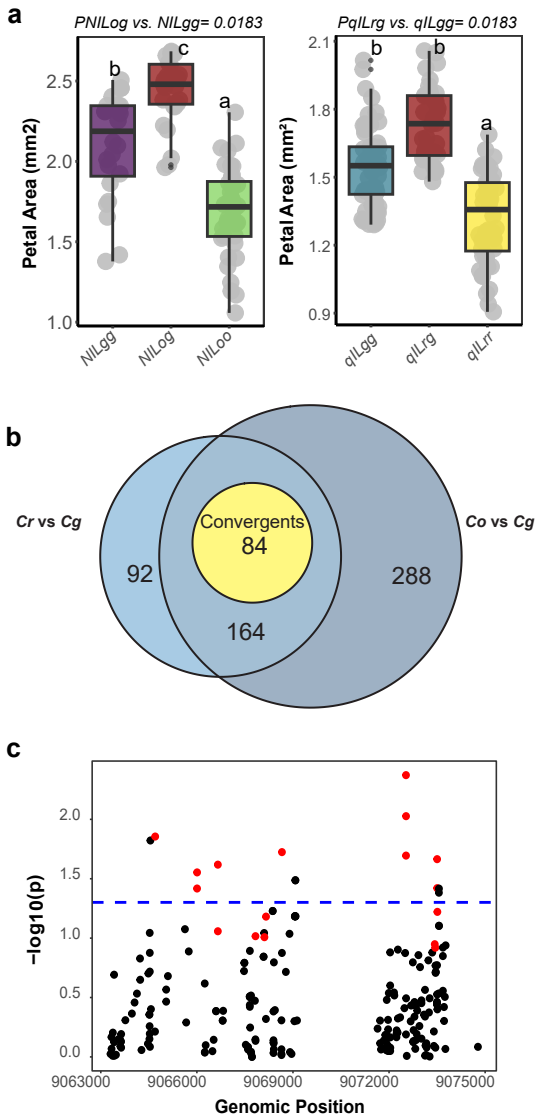

Fig. 5. Standing genetic variation in Cg contribute to convergence.
a, Relationship between petal size and *JAG* genotypes in the *NILog* and *qILrg* lines. Data points are gray dots; boxplots show petal area distribution per genotype. Letters denote significant differences from Tukey tests after a mixed-effects model with plant as a random effect. Bonferroni-adjusted p-values compare heterozygotes to larger homozygotes. **b,** Venn diagram depicts lineage-specific and shared polymorphic sites between the two Capsella selfer lineages versus their outcrosser ancestor. Convergent polymorphisms, where the same allele was fixed in both of the selfers, are highlighted in yellow. **c,** Manhattan-like plot displays genotype-phenotype (petal length) associations and overdominant loci. Each point tests a genomic locus's association with petal length; the x-axis shows position; the y-axis shows -log10(p), significance from linear model testing genotype effect on the phenotype. The dashed line marks p=0.05. Overdominant loci, where heterozygotes show the largest mean, are in red.
.